# HATS-9b AND HATS-10b: TWO COMPACT HOT JUPITERS IN FIELD 7 OF THE K2 MISSION[†]

R. Brahm[1,2], A. Jordán[1,2], J. D. Hartman[3], G. Á. Bakos[3,*,**], D. Bayliss[4,5], K. Penev[3], G. Zhou[5], S. Ciceri[6], M. Rabus[1,6], N. Espinoza[1,2], L. Mancini[6], M. de Val-Borro[3], W. Bhatti[3], B. Sato[7], T. G. Tan[8], Z. Csubry[3], L. Buchhave[9], T. Henning[6], B. Schmidt[5], V. Suc[1], R. W. Noyes[9], I. Papp[10], J. Lázár[10], and P. Sári[10]

*Draft version May 15, 2015*

## ABSTRACT

We report the discovery of two transiting extrasolar planets by the HATSouth survey. HATS-9b orbits an old ($10.8 \pm 1.5$ Gyr) V=13.3 G dwarf star, with a period $P \approx 1.9153$ d. The host star has a mass of $1.03\,M_\odot$, radius of $1.503\,R_\odot$ and effective temperature $5366 \pm 70$ K. The planetary companion has a mass of $0.837\,M_J$, and radius of $1.065\,R_J$ yielding a mean density of $0.85\,\mathrm{g\,cm^{-3}}$. HATS-10b orbits a V=13.1 G dwarf star, with a period $P \approx 3.3128$ d. The host star has a mass of $1.1\,M_\odot$, radius of $1.11\,R_\odot$ and effective temperature $5880 \pm 120$ K. The planetary companion has a mass of $0.53\,M_J$, and radius of $0.97\,R_J$ yielding a mean density of $0.7\,\mathrm{g\,cm^{-3}}$. Both planets are compact in comparison with planets receiving similar irradiation from their host stars, and lie in the nominal coordinates of Field 7 of K2 but only HATS-9b falls on working silicon. Future characterization of HATS-9b with the exquisite photometric precision of the *Kepler* telescope may provide measurements of its reflected light signature.

*Subject headings:* planetary systems — stars: individual ( HATS-9, GSC 6305-02502, HATS-10, GSC 6311-00085 ) techniques: spectroscopic, photometric

## 1. INTRODUCTION

Our current understanding of the structure and orbital evolution of extrasolar giant planets has been, to a large degree, informed by the characterization of transiting planetary systems. Besides the determination of the planet radius, true mass, and bulk density, follow-up studies of transiting extrasolar planets (TEPs) allow the extraction of valuable information, like the spin-orbit angle and the properties and composition of the planetary atmospheres, that are not be easily recovered unless the orbital plane is favorably oriented such that the planet eclipses its host star.

Detections of giant TEPs, mostly driven by transiting ground based surveys like SuperWASP (Pollacco et al. 2006) and HATNet (Bakos et al. 2004), have revealed a large number of systems in the region of parameter space with $R_p > 0.8R_J$, $M_p > 0.4M_J$, P<5 d and FGK-type host stars. The measured properties of these systems, coupled with subsequent follow-up studies, have been fundamental for testing formation and interior models of these giant planets, which are known as hot Jupiters.

New ground-based transiting surveys like HATSouth (Bakos et al. 2013) have been designed with the goal of expanding the parameter space of well characterized TEPs by detecting planets with smaller radii ($R_p < 0.4R_J$) and/or longer periods ($P > 10$ days). In the process of searching for these kinds of planets, new hot Jupiters are detected which contribute to enlarging the sample of known systems. Even though many hot Jupiters are already known, more are still needed to make headway into understanding their physical properties, e.g. a firm understanding of the mechanism that causes some hot Jupiters to have inflated radii (e.g. HAT-P-32b and HAT-P-33b, Hartman et al. 2011).

New planet discoveries around bright stars, accessible by follow-up facilities are especially valuable given the wealth of detailed studies that they can be subject to. Indeed, some of the most analyzed and characterized giant TEPs are three planets (TrES-2b, HAT-P-7b and HAT-P-11b) that were detected by ground-based surveys (Pál et al. 2008; Bakos et al. 2010; O'Donovan et al. 2006) and later observed by NASA's *Kepler* mission (Borucki et al. 2010). Even though the primary goal of *Kepler*

[1] Instituto de Astrofísica, Facultad de Física, Pontificia Universidad Católica de Chile, Av. Vicuña Mackenna 4860, 7820436 Macul, Santiago, Chile; rbrahm@astro.puc.cl
[2] Millennium Institute of Astrophysics, Av. Vicuña Mackenna 4860, 7820436 Macul, Santiago, Chile
[3] Department of Astrophysical Sciences, Princeton University, NJ 08544, USA
[*] Alfred P. Sloan Research Fellow
[**] Packard Fellow
[4] Observatoire Astronomique de l'Université de Genève, 51 ch. des Maillettes, 1290 Versoix, Switzerland
[5] The Australian National University, Canberra, Australia
[6] Max Planck Institute for Astronomy, Koenigstuhl 17, 69117, Heidelberg, Germany
[7] Department of Earth and Planetary Sciences, Tokyo Institute of Technology, 2-12-1 Ookayama, Meguro-ku, Tokyo 152-8551
[8] Perth Exoplanet Survey Telescope, Perth, Australia
[9] Harvard-Smithsonian Center for Astrophysics, Cambridge, MA 02138 USA
[10] Hungarian Astronomical Association, Budapest, Hungary
[†] The HATSouth network is operated by a collaboration consisting of Princeton University (PU), the Max Planck Institute for Astronomy (MPIA), the Australian National University (ANU), and the Pontificia Universidad Católica de Chile (PUC). The station at Las Campanas Observatory (LCO) of the Carnegie Institute is operated by PU in conjunction with PUC, the station at the High Energy Spectroscopic Survey (H.E.S.S.) site is operated in conjunction with MPIA, and the station at Siding Spring Observatory (SSO) is operated jointly with ANU. Based in part on data collected at Subaru Telescope, which is operated by the National Astronomical Observatory of Japan. Based in part on observations made with the MPG 2.2 m Telescope at the ESO Observatory in La Silla. This paper uses observations obtained with facilities of the Las Cumbres Observatory Global Telescope. Based on observations obtained with the Apache Point Observatory 3.5-meter telescope, which is owned and operated by the Astrophysical Research Consortium.

satellite was the detection of planets near the habitable zone for estimating their frequency and distribution in our galaxy, the high photometric precision of *Kepler* allowed very detailed studies of the small population of giant planets on close orbits around moderately bright stars ($V < 14$) that fell in its field of view.

*Kepler* was able to detect secondary transits and phase variations on TrES-2b and HAT-P-7b (Esteves et al. 2013) which were useful in the study of their atmospherical properties, such as the determination of the geometric albedos and planetary phase curve offsets. Doppler beaming and ellipsoidal variations measured with *Kepler* also constrained the mass of those planets. In the case of HAT-P-11b, *Kepler* observations were useful in characterizing the activity of the K-type host star; and the analysis of crossing stellar spots allowed the determination of the spin-orbit misalignment of this system (Deming et al. 2011; Sanchis-Ojeda & Winn 2011). Simultaneous observations of the transits of HAT-P-11b by *Kepler* and *Spitzer* allowed also the detection of water vapor in the atmosphere of this Neptune-size planet (Fraine et al. 2014). Estimation of the planetary physical parameters depend strongly on the estimated stellar properties. In this regard, *Kepler* was also able to measure model independent stellar properties by the use of asteroseismology on the three mentioned systems (Christensen-Dalsgaard et al. 2010).

After the failure of two of its reaction wheels, the *Kepler* satellite is still working, but with a new observation strategy and a photometric precision within a factor of $\sim 2$ of the nominal Kepler mission performance (e.g., Vanderburg & Johnson 2014; Aigrain et al. 2015; Foreman-Mackey et al. 2015; Crossfield et al. 2015). This new mission concept, called K2 (Howell et al. 2014), will observe 10 fields, each for a period of approximately 70 days, and some of these fields lie in the Southern hemisphere. One of the limitations of K2 is that the number of stars that can be monitored in each field is substantially lower than for the original *Kepler* mission. For this reason, the preselection of targets, based on ground-based observations of K2 fields is especially important for an efficient use of the satellite.

In this work we present the discovery of HATS-9b and HATS-10b, two hot Jupiters discovered by the HATSouth survey which are located in the nominal coordinates of Field 7 of K2 mission. In Section 2 we summarize the observations that allowed the discovery and confirmation of these planets. In Section 3 we show the global analysis of the spectroscopic and photometric data that confirmed the planetary nature of the transiting candidates and also rejected blend scenarios that can mimic the photometric and radial velocity signals. Our findings are discussed in Section 4.

## 2. OBSERVATIONS

### 2.1. *Photometric detection*

HATS-9 and HATS-10 were identified as transiting planetary host candidates after obtaining $\sim 10000$ images of the same field with three stations on the three HATSouth observing sites. The number of photometric observations that were taken for each star on each of the HATSouth stations is indicated in Table 1, where it can be seen that in both cases $\sim 45\%$ of the observa-

tions came from the HATSouth station located at Las Campanas Observatory (LCO).

The HATSouth observations consist of four-minute Sloan $r$-band exposures obtained with 24 Takahashi E180 astrographs (18cm aperture) coupled to Apogee 4Kx4K U16M ALTA CCDs. Readout times are of the order of one minute which results in a cadence of about 5 minutes. Detailed descriptions of the image processing steps and the candidate identification procedures of HATSouth data can be found in Bakos et al. (2013) and Penev et al. (2013). Briefly, after applying aperture photometry on the images, the light curves generated are detrended using external parameter decorrelation (EPD) and trend filtering algorithm (TFA Kovács et al. 2005). Periodic transits on the detrended light curves are then searched using Box-fitted Least Squares (BLS) algorithm (Kovács et al. 2002).

Figure 1 shows the phase-folded detection light curves of HATS-9b and HATS-10b, where a clear $\sim 10$ mmag flat-bottom transit can be observed in both cases.

### 2.2. *Spectroscopic Observations*

Transit-like light curves can be produced by different configurations of stellar binaries. Spectroscopic observations are required to reject false positives and to obtain the orbital parameters and masses of the true planets. Due to the great number of HATSouth candidates and the limited available observing time on spectroscopic facilities, this follow-up is performed in a two-step procedure as we now describe. All spectroscopic observations are summarized in Table 2.

First, initial spectra are acquired (with either low resolution, or low S/N) to make a rough estimation of the stellar parameters, identifying spectra composed of more than one star, and measuring RV variations produced by stellar mass companions. HATS-9 was observed with WIFeS (Dopita et al. 2007) on the ANU 2.3m telescope, obtaining $T_{\rm eff\star}$=5821 $\pm$ 300 K, $\log g_\star$=3.9 $\pm$ 0.3 [Fe/H]=0.5 $\pm$ 0.5; and with ARCES on the APO 3.5m obtaining $T_{\rm eff\star}$=5692 $\pm$ 50 K, $\log g_\star$=4.14 $\pm$ 0.1 [Fe/H]=0.5 $\pm$ 0.08. Both estimates of stellar parameters were consistent with a G-type dwarf, but the sub-solar surface gravity value points towards a slightly evolved system. Details on the observing strategy, reduction methods and the processing of the spectra for WIFeS can be found in Bayliss et al. (2013). The ARCES observation was carried out using the $1''\!.6 \times 3''\!.2$ slit yielding an echelle spectrum with 107 orders covering the wavelength range 3200–10000Å at a resolution of $\Delta\lambda/\lambda \sim 31500$. A single ThAr lamp spectrum was obtained immediately following the science exposure with the telescope still pointed toward HATS-9. The science observation was reduced to a wavelength-calibrated spectrum using the standard IRAF echelle package[1], and analyzed using the Spectral Parameter Classification (SPC) program (Buchhave et al. 2012) to determine the radial velocity and stellar atmospheric parameters.

Reconnaissance spectroscopy was performed for HATS-10 using the echelle spectrograph mounted on

---

[1] IRAF is distributed by the National Optical Astronomy Observatories, which are operated by the Association of Universities for Research in Astronomy, Inc., under cooperative agreement with the National Science Foundation.
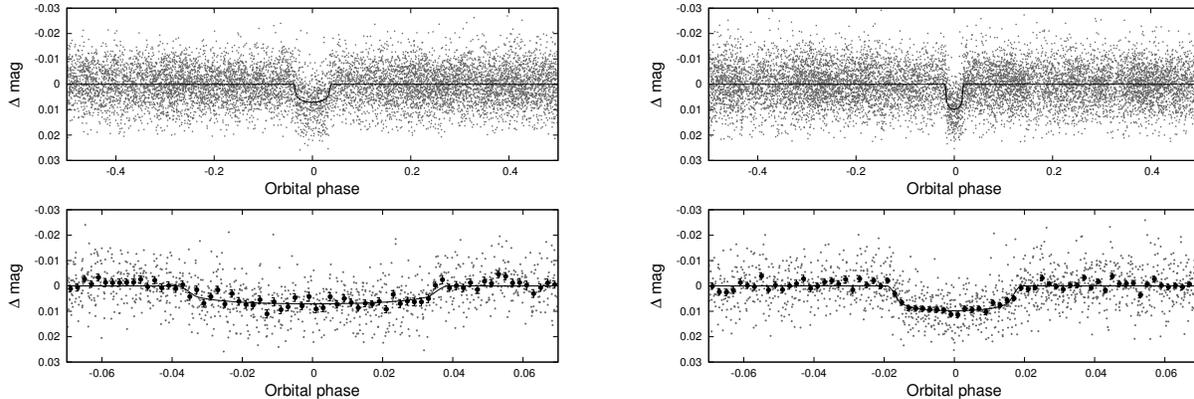
**Figure 1.** Phase-folded unbinned HATSouth light curves for HATS-9 (left) and HATS-10 (right). In each case we show two panels. The top panel shows the full light curve, while the bottom panel shows the light curve zoomed-in on the transit. The solid lines show the model fits to the light curves. The dark filled circles in the bottom panels show the light curves binned in phase with a bin size of 0.002.

**Table 1**
Summary of photometric observations

| Instrument/Field[a] | Date(s) | # Images | Cadence[b] (sec) | Filter | Precision[c] (mmag) |
|---|---|---|---|---|---|
| **HATS-9** | | | | | |
| HS-1/G579 | 2010 Mar–2011 Aug | 4317 | 300 | $r$ band | 6.9 |
| HS-3/G579 | 2010 Mar–2011 Aug | 2138 | 303 | $r$ band | 7.6 |
| HS-5/G579 | 2010 Sep–2011 Aug | 2784 | 303 | $r$ band | 6.9 |
| FTS | 2013 Apr 11 | 134 | 80 | $i$ band | 1.4 |
| PEST | 2013 May 31 | 186 | 130 | $R_C$ band | 3.4 |
| **HATS-10** | | | | | |
| HS-1/G579 | 2009 Sep–2011 Aug | 4389 | 301 | $r$ band | 7.3 |
| HS-3/G579 | 2010 Mar–2011 Aug | 2596 | 303 | $r$ band | 7.2 |
| HS-5/G579 | 2011 Mar–2011 Aug | 3297 | 303 | $r$ band | 7.8 |
| CTIO 0.9m | 2012 Aug 29 | 69 | 213 | $z$ band | 2.3 |
| FTS | 2013 Apr 05 | 142 | 63 | $i$ band | 4.3 |
| GROND | 2013 Jun 14 | 92 | 156 | $g$ band | 0.8 |
| GROND | 2013 Jun 14 | 88 | 156 | $r$ band | 1.3 |
| GROND | 2013 Jun 14 | 94 | 156 | $i$ band | 0.7 |
| GROND | 2013 Jun 14 | 89 | 156 | $z$ band | 0.8 |
| PEST | 2013 Jun 27 | 145 | 130 | $R_C$ band | 4.6 |

[a] For HATSouth data we list the HATSouth unit and field name from which the observations are taken. HS-1 and -2 are located at Las Campanas Observatory in Chile, HS-3 and -4 are located at the H.E.S.S. site in Namibia, and HS-5 and -6 are located at Siding Spring Observatory in Australia. Each field corresponds to one of 838 fixed pointings used to cover the full $4\pi$ celestial sphere. All data from a given HATSouth field are reduced together, while detrending through External Parameter Decorrelation (EPD) is done independently for each unique field+unit combination.

[b] The median time between consecutive images rounded to the nearest second. Due to weather, the day–night cycle, guiding and focus corrections, and other factors, the cadence is only approximately uniform over short timescales.

[c] The RMS of the residuals from the best-fit model.

the du Pont 2.5m telescope at Las Campanas Observatory. One observation using the $1'' \times 4''$ slit ($\Delta\lambda/\lambda \sim 40000$) was enough to confirm that HATS-10 has a single lined spectrum with the following stellar parameters: $T_{\mathrm{eff}\star}$=6100 ± 100 K, $\log g_\star$=4.6 ± 0.5 [Fe/H]=0.0 ± 0.5, $v \sin i$=5.0 ± 2.0 km/s. This spectrum was reduced and analysed with an automated pipeline developed to deal with data coming from a host of different echelle spectrographs (Brahm et al. in prep.). The pipeline for DuPont is very similar to the ones we have previously detailed for Coralie and FEROS data in Jordán et al. (2014).

Once both candidates were identified as single-lined late-type dwarfs, spectra from high precision instruments were required to measure RV variations with high precision (< 30 m/s) in order to measure the mass of the substellar companions and obtain the orbital parameters. HATS-9 and HATS-10 were observed several times with

Coralie (Queloz et al. 2001) on the 1.2m Euler telescope, FEROS (Kaufer & Pasquini 1998) on the 2.2m MPG telescope, and HDS on the 8m Subaru telescope (Noguchi et al. 2002). Coralie and FEROS data were processed with the pipeline described in Jordán et al. (2014), where RV values are obtained using the cross correlation technique against a binary mask and bisector span (BS) measurements are computed from the cross-correlation peak following Queloz et al. (2001). HDS RVs were measured using the procedure detailed in Sato et al. (2002, 2012) which are in turn based on the method of Butler et al. (1996) while BS values were obtained following Bakos et al. (2007).

Phased high-precision RV and BS measurements are shown for each system in Figure 2 and the data are listed in Table 3. Both candidates show RV variations in phase with photometric ephemeris, however for HATS-10

the residuals are higher than expected. This deviation
can be partly explained by moonlight contamination in
5 spectra acquired with Coralie in August 2013 which
are marked with crosses in Figure 2. There are no sig-
nificant correlations between RV and BS variations and
thus we conclude the RV variations are not produced
by stellar activity. The 95% confidence interval for the
Pearson correlation coefficient between RV and BS was
computed for both candidates using a bootstrap proce-
dure. The confidence intervals are [-0.57,0.07] and [-0.43,
0.37] for HATS-9 and HATS-10, respectively. The indi-
vidual FEROS spectra were median combined for both
candidates to perform a precise estimation of the stellar
parameters.

### 2.3. *Photometric follow-up observations*

In order to confirm the occurrence of the transits and
to better constrain the orbital and physical parameters
of the companions, higher precision light curves for both
candidates were acquired using several telescopes around
the globe. Table 1 summarizes the key aspects of this
photometric follow-up, including the dates of the obser-
vations, the cadence and the filter.

Two partial transits of HATS-9 were detected using
the 0.3m Perth Exoplanet Survey Telescope (PEST) and
the Spectral camera on the 2m Faulkes Telescope South
(FTS), part of Las Cumbres Observatory Global Tele-
scope (LCOGT). Results of these observations are pre-
sented in Table 4 and shown in Figure 3. Two partial
transits of HATS-10 were observed with FTS and the
CTIO 0.9m telescope. Another two full transits were
measured with PEST and the GROND instrument on
the MPG 2.2 m. These HATS-10 light curves are shown
in Figure 4. All the facilities used for high precision pho-
tometric follow-up have been previously used by HAT-
South; the instrument specifications, observation strate-
gies and reduction procedures adopted can be found in
Bayliss et al. (2013), Zhou et al. (2014b), Hartman et al.
(2014) and Mohler-Fischer et al. (2013) for FTS, PEST,
CTIO 0.9m, and GROND, respectively.

**Table 2**
Summary of spectroscopy observations

| Instrument | UT Date(s) | # Spec. | Res. $\Delta\lambda/\lambda/1000$ | S/N Range[a] | $\gamma_{RV}$[b] $(\mathrm{km\,s^{-1}})$ | RV Precision[c] $(\mathrm{m\,s^{-1}})$ |
|---|---|---|---|---|---|---|
| **HATS-9** | | | | | | |
| APO 3.5 m/ARCES | 2012 Aug 25 | 1 | 31.5 | 27 | -11.5 | 500 |
| ANU 2.3 m/WiFeS | 2012 Sep 8 | 1 | 3 | 140 | ⋯ | ⋯ |
| Euler 1.2 m/Coralie | 2012 Nov 6–10 | 4 | 60 | 14–20 | -10.634 | 37 |
| MPG 2.2 m/FEROS | 2012 Aug–2013 May | 9 | 48 | 32–76 | -10.653 | 32 |
| Subaru 8 m/HDS | 2012 Sep 19 | 3 | 60 | 100–114 | ⋯ | ⋯ |
| Subaru 8 m/HDS+I$_2$ | 2012 Sep 20–22 | 9 | 60 | 60–100 | ⋯ | 11 |
| **HATS-10** | | | | | | |
| du Pont 2.5 m/Echelle | 2013 Aug 21 | 1 | 40 | 48 | -29.2 | 500 |
| Euler 1.2 m/Coralie | 2012 Aug–2013 Aug | 12 | 60 | 17–23 | -28.131 | 68 |
| MPG 2.2 m/FEROS | 2013 Mar–Jul | 5 | 48 | 29–85 | -28.044 | 50 |
| Subaru 8 m/HDS | 2012 Sep 22 | 3 | 60 | 74–94 | ⋯ | ⋯ |
| Subaru 8 m/HDS+I$_2$ | 2012 Sep 19–21 | 9 | 60 | 41–99 | ⋯ | 14 |

[a] S/N per resolution element near 5180 Å.

[b] For Coralie and FEROS this is the systemic RV from fitting an orbit to the observations in Section 3.3. For ARCES and the du Pont Echelle it is the measured RV of the single observation. We do not provide this quantity for instruments for which only relative RVs are measured, or for WiFeS which was only used to measure stellar atmospheric parameters.

[c] For High-precision RV observations included in the orbit determination this is the RV residuals from the best-fit orbit, for other instruments used for reconnaissance spectroscopy this is an estimate of the precision.
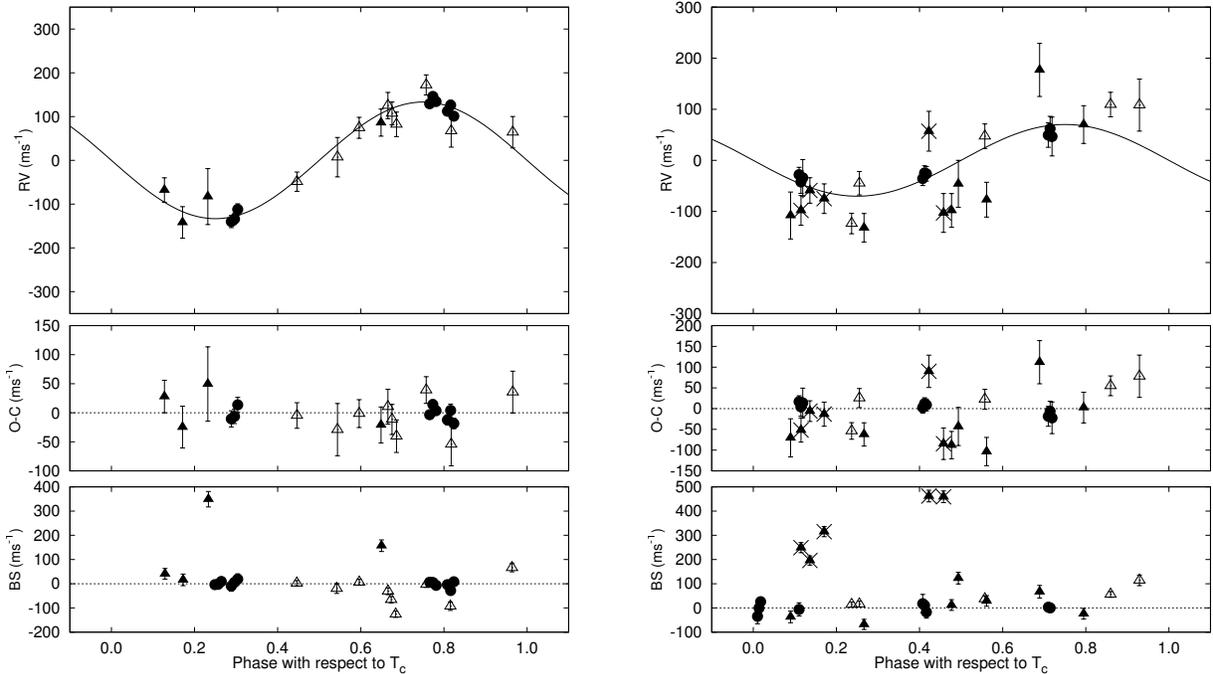


**Figure 2.** Phased high-precision RV measurements for HATS-9 (left), and HATS-10 (right) from HDS (filled circles), FEROS (open triangles), and Coralie (filled triangles). In each case we show three panels. The top panel shows the phased measurements together with our best-fit model (see Table 6) for each system. Zero-phase corresponds to the time of mid-transit. The center-of-mass velocity has been subtracted. The second panel shows the velocity $O-C$ residuals from the best fit. The error bars include the jitter terms listed in Table 6 added in quadrature to the formal errors for each instrument. The third panel shows the bisector spans (BS), with the mean value subtracted. Note the different vertical scales of the panels. RV measurements highly contaminated with moonlight are marked with crosses.

**Table 3**
Relative radial velocities and bisector spans for HATS-9 and HATS-10.

| BJD (2,456,000+) | RV[a] ($\mathrm{m\,s^{-1}}$) | $\sigma_{RV}$[b] ($\mathrm{m\,s^{-1}}$) | BS ($\mathrm{m\,s^{-1}}$) | $\sigma_{BS}$ ($\mathrm{m\,s^{-1}}$) | Phase | Instrument |
|---|---|---|---|---|---|---|
| **HATS-9** | | | | | | |
| 169.62456 | 82.24 | 28.00 | −126.0 | 13.0 | 0.686 | FEROS |
| 171.51911 | 107.24 | 26.00 | −66.0 | 13.0 | 0.675 | FEROS |
| 173.70707 | 67.24 | 37.00 | −93.0 | 17.0 | 0.817 | FEROS |
| 189.85616 | ⋯ | ⋯ | −3.6 | 13.0 | 0.249 | Subaru |
| 189.87089 | ⋯ | ⋯ | −2.3 | 11.0 | 0.257 | Subaru |
| 189.88561 | ⋯ | ⋯ | 9.6 | 9.2 | 0.264 | Subaru |
| 190.84576 | 129.27 | 7.39 | 6.2 | 13.4 | 0.766 | Subaru |
| 190.86048 | 146.04 | 8.17 | 5.3 | 10.0 | 0.773 | Subaru |
| 190.87520 | 134.32 | 7.39 | −6.7 | 13.6 | 0.781 | Subaru |
| 191.84685 | −139.82 | 13.91 | −9.6 | 21.4 | 0.288 | Subaru |
| 191.86157 | −133.96 | 12.35 | 6.0 | 13.5 | 0.296 | Subaru |
| 191.87633 | −112.04 | 12.85 | 19.1 | 21.9 | 0.304 | Subaru |
| 192.84272 | 112.22 | 8.57 | −3.7 | 18.5 | 0.808 | Subaru |
| 192.85745 | 126.06 | 10.89 | −28.3 | 16.3 | 0.816 | Subaru |
| 192.87217 | 100.81 | 9.05 | 8.0 | 8.8 | 0.824 | Subaru |
| 205.55663 | −48.76 | 22.00 | 2.0 | 11.0 | 0.446 | FEROS |
| 213.50471 | 74.24 | 24.00 | 6.0 | 12.0 | 0.596 | FEROS |
| 215.55235 | 125.24 | 30.00 | −31.0 | 14.0 | 0.665 | FEROS |
| 219.55921 | 172.24 | 23.00 | −3.0 | 12.0 | 0.757 | FEROS |
| 237.50625 | −67.84 | 28.00 | 41.0 | 22.0 | 0.128 | Coralie |
| 238.50417 | 86.16 | 31.00 | 157.0 | 24.0 | 0.649 | Coralie |
| 239.50502 | −141.84 | 36.00 | 16.0 | 24.0 | 0.171 | Coralie |
| 241.53678 | −82.84 | 64.00 | 349.0 | 32.0 | 0.232 | Coralie |
| 424.89567 | 64.24 | 36.00 | 66.0 | 17.0 | 0.965 | FEROS |
| 427.91875 | 7.24 | 45.00 | −20.0 | 20.0 | 0.544 | FEROS |
| **HATS-10** | | | | | | |
| 160.60805 | −132.00 | 28.00 | −68.0 | 21.0 | 0.267 | Coralie |
| 161.58511 | −77.00 | 34.00 | 29.0 | 22.0 | 0.561 | Coralie |
| 164.61796 | −98.00 | 33.00 | 12.0 | 22.0 | 0.477 | Coralie |
| 189.90597 | −27.97 | 14.29 | −6.1 | 27.3 | 0.110 | Subaru |
| 189.92069 | −42.32 | 22.31 | ⋯ | ⋯ | 0.115 | Subaru |
| 189.93541 | −34.14 | 35.70 | ⋯ | ⋯ | 0.119 | Subaru |
| 190.89115 | −35.74 | 13.59 | 17.7 | 38.3 | 0.408 | Subaru |
| 190.90587 | −24.73 | 14.10 | 10.6 | 18.6 | 0.412 | Subaru |
| 190.92060 | −26.35 | 14.32 | −17.0 | 25.1 | 0.416 | Subaru |
| 191.89225 | 49.44 | 23.96 | 3.2 | 15.3 | 0.710 | Subaru |
| 191.90697 | 62.06 | 24.16 | 0.2 | 17.3 | 0.714 | Subaru |
| 191.92170 | 46.62 | 38.06 | ⋯ | ⋯ | 0.719 | Subaru |
| 192.88724 | ⋯ | ⋯ | −34.5 | 31.0 | 0.010 | Subaru |
| 192.89965 | ⋯ | ⋯ | −0.2 | 23.1 | 0.014 | Subaru |
| 192.91206 | ⋯ | ⋯ | 25.9 | 15.7 | 0.018 | Subaru |
| 237.55535 | −46.00 | 46.00 | 123.0 | 24.0 | 0.493 | Coralie |
| 238.55388 | 70.00 | 37.00 | −24.0 | 22.0 | 0.795 | Coralie |
| 239.53128 | −108.00 | 46.00 | −37.0 | 24.0 | 0.090 | Coralie |
| 241.51608 | 177.00 | 52.00 | 67.0 | 26.0 | 0.689 | Coralie |
| 375.90634 | −44.76 | 23.00 | 16.0 | 12.0 | 0.255 | FEROS |
| 376.90643 | 47.24 | 24.00 | 37.0 | 12.0 | 0.557 | FEROS |
| 377.90816 | 109.24 | 24.00 | 56.0 | 12.0 | 0.860 | FEROS |
| 427.83173 | 108.24 | 51.00 | 114.0 | 22.0 | 0.929 | FEROS |
| 491.79404 | −123.76 | 20.00 | 14.0 | 10.0 | 0.236 | FEROS |
| 524.51947[c] | −98.00 | 29.00 | 249.0 | 21.0 | 0.115 | Coralie |
| 524.59002[c] | −59.00 | 25.00 | 196.0 | 19.0 | 0.136 | Coralie |
| 524.70382[c] | −75.00 | 29.00 | 315.0 | 21.0 | 0.170 | Coralie |
| 525.53878[c] | 57.00 | 39.00 | 462.0 | 24.0 | 0.422 | Coralie |
| 525.65573[c] | −103.00 | 38.00 | 459.0 | 24.0 | 0.458 | Coralie |

**Note**. — Note that for the iodine-free template exposures we do not measure the RV but do measure the BS and S index. Such template exposures can be distinguished by the missing RV value. The Subaru/HDS observations of HATS-10 without BS measurements have too low S/N in the $I_2$-free blue spectral region to pass our quality threshold for calculating accurate BS values.

[a] The zero-point of these velocities is arbitrary. An overall offset $\gamma_{\mathrm{rel}}$ fitted independently to the velocities from each instrument has been subtracted.

[b] Internal errors excluding the component of astrophysical jitter considered in Section 3.3.

[b] Coralie observations acquired in August 2013 were contaminated with moonlight.
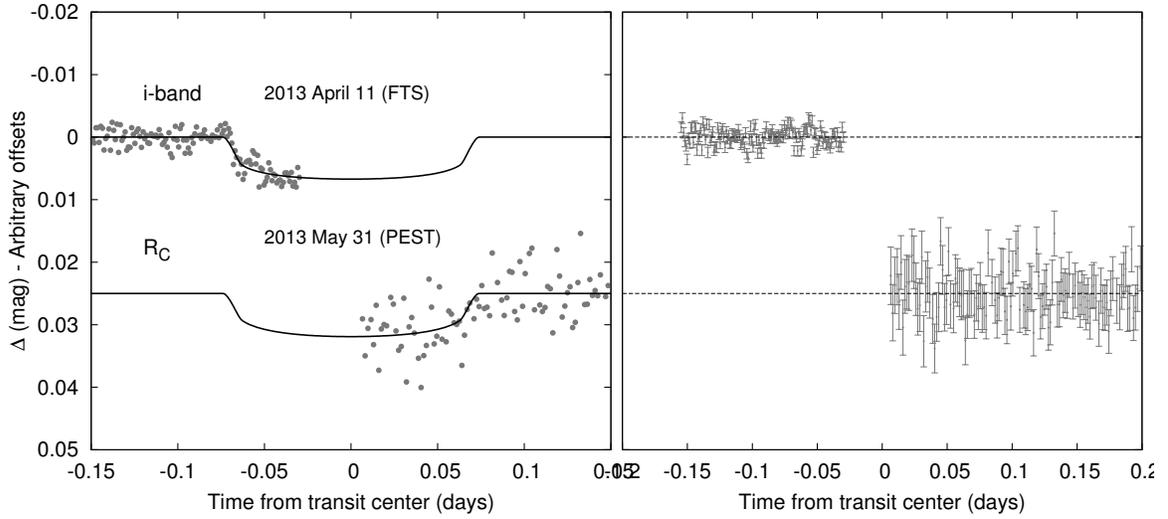
**Figure 3.** Left: Unbinned transit light curves for HATS-9. The light curves have been corrected for quadratic trends in time fitted simultaneously with the transit model. The dates of the events, filters and instruments used are indicated. The second curve is displaced vertically for clarity. Our best fit from the global modeling described in Section 3.3 is shown by the solid lines. Right: residuals from the fits are displayed in the same order as the left curves. The error bars represent the photon and background shot noise, plus the readout noise.
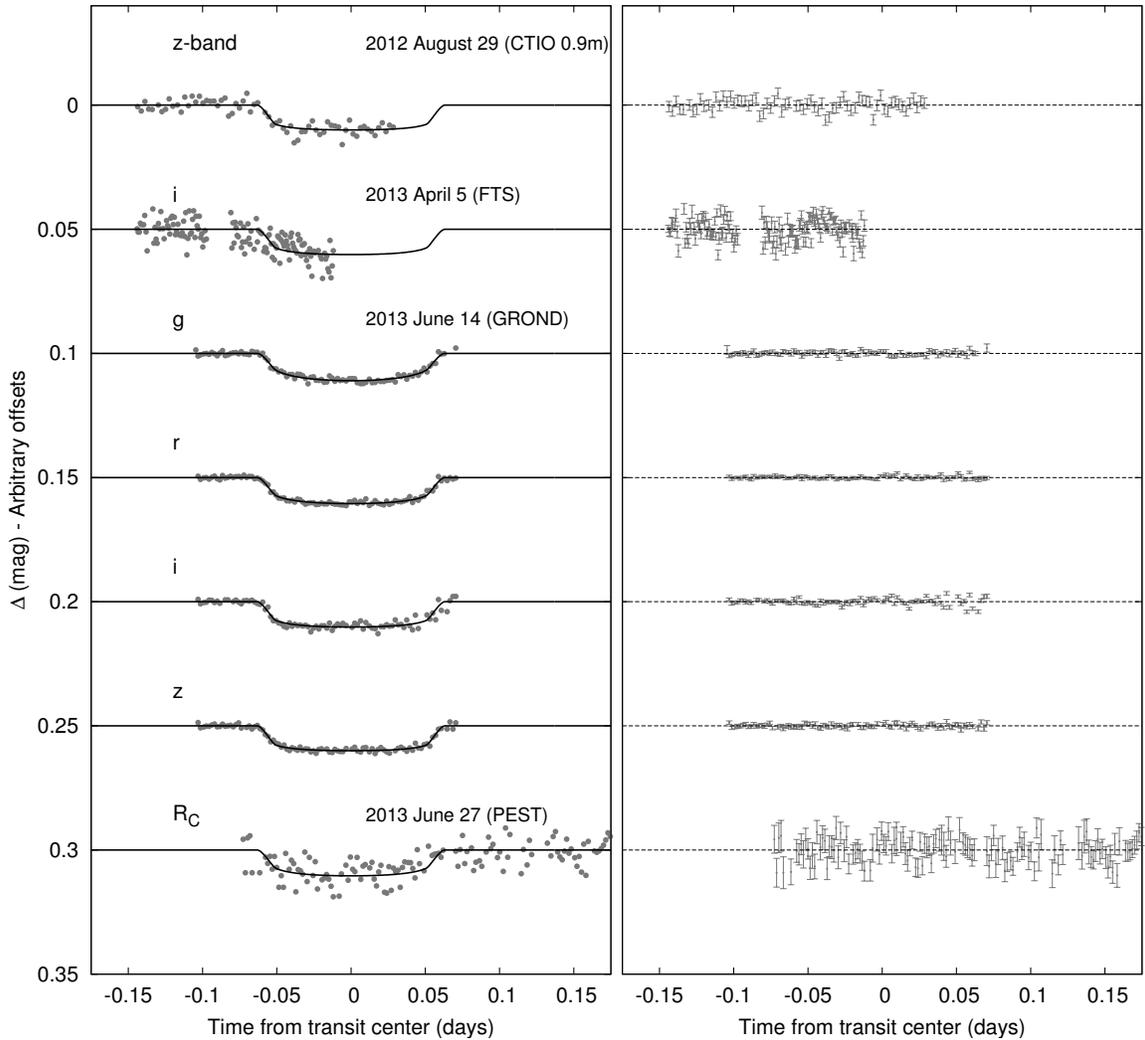


**Figure 4.** Similar to Figure 3; here we show the follow-up light curves for HATS-10.

## 3. ANALYSIS

### 3.1. *Properties of the parent star*

We determine precise stellar parameters for HATS-9 and HATS-10 using a new code called ZASPE (Zonal Atmospherical Stellar Parameter Estimator) on median combined FEROS spectra. The detailed structure and performance of ZASPE will be presented elsewhere (Brahm et al. in preparation), but in summary ZASPE is a Python-based code that computes the $\chi^2$ between the observed spectra and the PHOENIX grid of synthetic spectra (Husser et al. 2013) only on the most sensitive spectral zones to each stellar parameter. The optimal set of stellar parameters ($T_{\rm eff\star}$, $\log g_\star$, [Fe/H] and $v \sin i$) is found iteratively and the sensitive zones are determined in each iteration. One of the most novel features of ZASPE is that the errors on the stellar parameters are computed from the data itself and include the systematic mismatches between the observations and the best fitted model. We have validated the results of ZASPE against a set of stars with interferometrically determined stellar parameters (Boyajian et al. 2012) and which have publicly available FEROS spectra. Results of this comparison are shown in Figure 5. The resulting parameters for HATS-9 are: $T_{\rm eff\star}$=5363 $\pm$ 90 K, $\log g_\star$=3.97 $\pm$ 0.2, [Fe/H]=0.33 $\pm$ 0.09, $v \sin i$=4.67 $\pm$ 0.5 km/s; while for HATS-10 we get: $T_{\rm eff\star}$=5974 $\pm$ 110 K, $\log g_\star$=4.44 $\pm$ 0.13, [Fe/H]=0.19 $\pm$ 0.07, $v \sin i$=5.66 $\pm$ 0.5 km/s.

These sets of stellar parameters were refined using the information contained in the transit light-curves. The stellar mean density ($\rho_\star$) can be computed directly from one of the light-curve model parameters ($a/R_\star$) and the period and eccentricity of the orbit by using Kepler's third law with only a slight dependence on the stellar parameters through the limb-darkening coefficients (Sozzetti et al. 2007). The spectroscopically determined $T_{\rm eff\star}$ and [Fe/H] were coupled with $\rho_\star$ and Yonsei-Yale stellar evolution models (Y2; Yi et al. 2001) to determine the stellar physical parameters ($R_\star$, $M_\star$ and the age of the star), which were used to compute a new and more precise estimation of $\log g_\star$ for HATS-9 ($\log g_\star$=4.12 $\pm$ 0.04) and HATS-10 ($\log g_\star$=4.38 $\pm$ 0.03). A new set of $T_{\rm eff\star}$, [Fe/H], $v \sin i$ was determined using ZASPE with $\log g_\star$ fixed to the precise values obtained by modeling the light curves, followed by a new estimation of $\rho_\star$ and a new modeling of stellar isochrones. The new set of stellar parameters fixing $\log g_\star$, which are the ones we adopted for further analysis, were consistent with the initial values quoted in the previous paragraph and are listed in Table 5, where distances are determined by comparing the measured broad-band photometry listed in that table to the predicted magnitudes in each filter from the isochrones. We assume a $R_V = 3.1$ extinction law from Cardelli et al. (1989) to determine the extinction. The $1\sigma$ and $2\sigma$ confidence ellipsoids in $T_{\rm eff\star}$ and $\rho_\star$ are plotted in Figure 6 for both planet hosts, along with the Y2 isochrones for the ZASPE determined [Fe/H]. We find that HATS-9 is a $1.030 \pm 0.039\ M_\odot$, $1.503^{+0.101}_{-0.043}\ R_\odot$, quite evolved ($10.8 \pm 1.5$ Gyr) star, while HATS-10 is a $1.101 \pm 0.054\ M_\odot$, $1.105^{+0.055}_{-0.040}\ R_\odot$ main-sequence star.

We attempted to measure the Lithium absorption line at 6707.8 Å for testing the age estimation of HATS-9 but the quality of our spectra was only enough to rule out a strong absorption feature.

### 3.2. *Excluding blend scenarios*

In order to exclude blend scenarios we carried out a blend analysis of the observations following Hartman et al. (2012). For HATS-9 we find that scenarios involving blends between a stellar eclipsing binary and a foreground or background star can be ruled out with greater than $5\sigma$ confidence based on the photometric data alone. The primary constraint in this case is the lack of out-of-transit variations seen in the HATSouth light curve. Due to the short orbital period, the best-fit blend model which reproduces the shape of the transit has a $\sim 1$ mmag amplitude ellipsoidal variation, and a $\sim 0.5$ mmag deep secondary eclipse, neither of which are detected in the HATSouth observations. Moreover the Subaru/HDS observations of HATS-9 show no significant bisector span variation (the RMS scatter of the BS measurements is $12\,{\rm m\,s^{-1}}$) providing further evidence that the system is not a blended eclipsing binary. For HATS-10 the photometric observations can be fit by a G+M star eclipsing binary blended with another G star that is slightly brighter than the primary in the eclipsing system. Based on the difference in $\chi^2$, this model is indistinguishable from a single G star with a transiting planet. We simulated spectra for blend models that could plausibly fit the photometric observations, finding that it all cases the blended systems would have easily been detected as having composite spectra. They also would produce RV and BS variations of several $\rm km\,s^{-1}$, whereas the observed RV variation is $67 \pm 10\,{\rm m\,s^{-1}}$, and the Subaru/HDS BS scatter is only $18\,{\rm m\,s^{-1}}$. We conclude that neither HATS-9 nor HATS-10 is a blended eclipsing binary system. As is often the case, however, we are not able to rule out the possibility that either transiting planet system has a fainter stellar-mass companion. For both systems a stellar companion of any mass, up to the mass of the planet-hosting star, is possible. If a massive stellar companion is present in a given system, the true planet radius would be up to $\sim 60\%$ larger than inferred here. The planet mass would also be larger. High resolution adaptive optics imaging, and/or long-term RV observations are needed to determine whether either system has a stellar companion (e.g. Howell et al. 2011; Horch et al. 2014; Everett et al. 2015).

### 3.3. *Global modeling of the data*

We modeled the HATSouth photometry, the follow-up photometry, and the high-precision RV measurements following Pál et al. (2008); Bakos et al. (2010); Hartman et al. (2012). We fit Mandel & Agol (2002) transit models to the light curves, allowing for a dilution of the HATSouth transit depth as a result of blending from neighboring stars and over-correction by the trend-filtering method. For the follow-up light curves we include a quadratic trend in time in our model for each event to correct for systematic errors in the photometry. We fit Keplerian orbits to the RV curves allowing the zero-point for each instrument to vary independently in the fit, and allowing for RV jitter which we we also vary as a free parameter for each instrument.

We used a Differential Evolution Markov Chain Monte Carlo procedure (ter Braak 2006; Eastman et al. 2013)

**Table 4**
Light curve data for HATS-9 and HATS-10.

| Object[a] | BJD[b] (2,400,000+) | Mag[c] | $\sigma_{\mathrm{Mag}}$ | Mag(orig)[d] | Filter | Instrument |
|---|---|---|---|---|---|---|
| HATS-9 | 55744.07098 | −0.00037 | 0.00552 | 0.00000 | $r$ | HS |
| HATS-9 | 55749.81701 | −0.00018 | 0.00572 | 0.00000 | $r$ | HS |
| HATS-9 | 55780.46237 | 0.00906 | 0.00604 | 0.00000 | $r$ | HS |
| HATS-9 | 55767.05534 | −0.01086 | 0.00553 | 0.00000 | $r$ | HS |
| HATS-9 | 55696.18926 | 0.01787 | 0.00581 | 0.00000 | $r$ | HS |
| HATS-9 | 55657.88321 | −0.00168 | 0.00549 | 0.00000 | $r$ | HS |
| HATS-9 | 55726.83440 | 0.00055 | 0.00619 | 0.00000 | $r$ | HS |
| HATS-9 | 55680.86732 | 0.01840 | 0.00534 | 0.00000 | $r$ | HS |
| HATS-9 | 55788.12454 | 0.00811 | 0.00716 | 0.00000 | $r$ | HS |
| HATS-9 | 55776.63287 | −0.00411 | 0.00550 | 0.00000 | $r$ | HS |

**Note**. — This table is available in a machine-readable form in the online journal. A portion is shown here for guidance regarding its form and content.
[a] Either HATS-9, or HATS-10.
[b] Barycentric Julian Date is computed directly from the UTC time without correction for leap seconds.
[c] The out-of-transit level has been subtracted. For observations made with the HATSouth instruments (identified by "HS" in the "Instrument" column) these magnitudes have been corrected for trends using the EPD and TFA procedures applied *prior* to fitting the transit model. This procedure may lead to an artificial dilution in the transit depths. For HATS-9 our fit is consistent with no dilution, for HATS-10 the HATSouth transit depth is ∼ 93% that of the true depth. For observations made with follow-up instruments (anything other than "HS" in the "Instrument" column), the magnitudes have been corrected for a quadratic trend in time fit simultaneously with the transit.
[d] Raw magnitude values without correction for the quadratic trend in time. These are only reported for the follow-up observations.
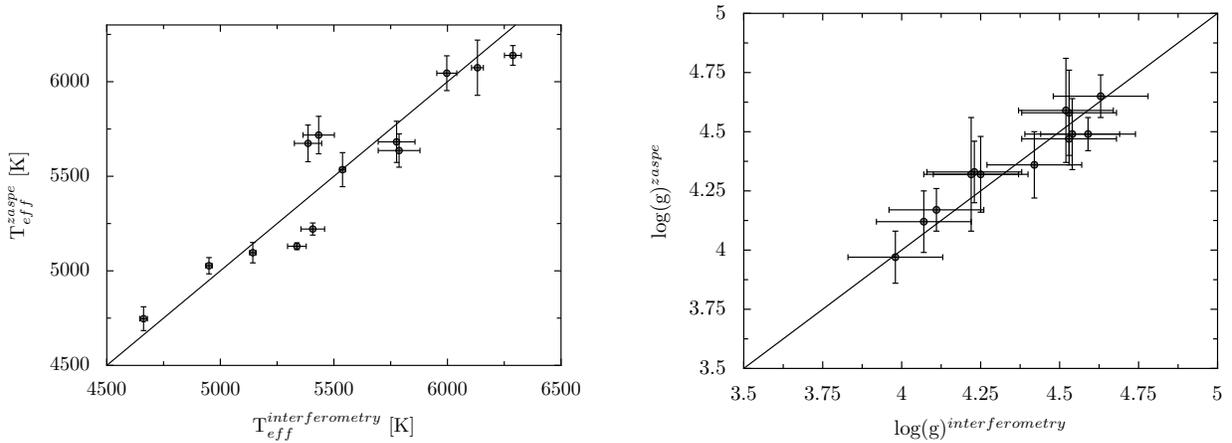


**Figure 5.** (Left): Comparison between $T_{eff}$ values obtained with ZASPE and the ones derived from interferometric information. (Right): Comparison between log(g) values obtained with ZASPE and the ones derived from interferometric information.
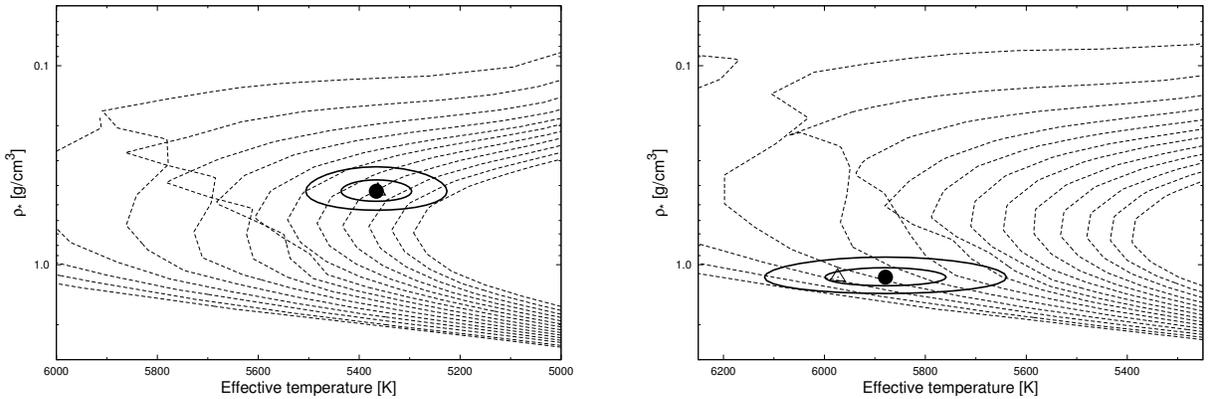


**Figure 6.** Model isochrones from Yi et al. (2001) for the measured metallicities of HATS-9 (left) and HATS-10 (right). In each case we show models for ages of 0.2 Gyr and 1.0 to 14.0 Gyr in 1.0 Gyr increments (ages increasing from left to right). The adopted values of $T_{\mathrm{eff}\star}$ and $\rho_\star$ are shown together with their 1$\sigma$ and 2$\sigma$ confidence ellipsoids. The initial values of $T_{\mathrm{eff}\star}$ and $\rho_\star$ from the first ZASPE and light curve analyzes are represented with a triangle.

to explore the fitness landscape and to determine the posterior distribution of the parameters.

**Table 5**
Stellar parameters for HATS-9 and HATS-10

| Parameter | HATS-9 Value | HATS-10 Value | Source |
|---|---|---|---|
| Astrometric properties and cross-identifications | | | |
| 2MASS-ID......... | 2MASS 19231442-2009587 | 2MASS 19371363-2212161 | |
| GSC-ID ........... | GSC 6305-02502 | GSC 6311-00085 | |
| R.A. (J2000)....... | $19^h23^m14.28s$ | $19^h37^m13.80s$ | 2MASS |
| Dec. (J2000)....... | $-20°09'58.7''$ | $-22°12'16.1''$ | 2MASS |
| $\mu_{R.A.}$ (mas yr$^{-1}$) | $0.3 \pm 4.3$ | $3.1 \pm 1.3$ | UCAC4 |
| $\mu_{Dec.}$ (mas yr$^{-1}$) | $-1.9 \pm 2.8$ | $-3.2 \pm 1.6$ | UCAC4 |
| Spectroscopic properties | | | |
| $T_{eff\star}$ (K)........... | $5366 \pm 70$ | $5880 \pm 120$ | ZASPE[a] |
| [Fe/H] ............. | $0.340 \pm 0.050$ | $0.15 \pm 0.10$ | ZASPE |
| $v \sin i$ (km s$^{-1}$) .... | $4.58 \pm 0.90$ | $5.68 \pm 0.70$ | ZASPE |
| $v_{mac}$ (km s$^{-1}$) ..... | 4.6 | 3.8 | Assumed[b] |
| $v_{mic}$ (km s$^{-1}$)...... | 1.0 | 1.0 | Assumed[c] |
| $\gamma_{RV}$ (km s$^{-1}$) ...... | $-10.644 \pm 0.013$ | $-28.088 \pm 0.024$ | Coralie,FEROS |
| Photometric properties | | | |
| $B$ (mag).......... | $14.080 \pm 0.010$ | $13.820 \pm 0.010$ | APASS[d] |
| $V$ (mag).......... | $13.276 \pm 0.010$ | $13.113 \pm 0.010$ | APASS[d] |
| $g$ (mag)........... | $13.629 \pm 0.010$ | $13.448 \pm 0.010$ | APASS[d] |
| $r$ (mag)........... | $13.072 \pm 0.030$ | $12.967 \pm 0.010$ | APASS[d] |
| $i$ (mag) ........... | $12.865 \pm 0.010$ | $12.781 \pm 0.010$ | APASS[d] |
| $J$ (mag) .......... | $11.885 \pm 0.022$ | $11.866 \pm 0.024$ | 2MASS |
| $H$ (mag).......... | $11.558 \pm 0.027$ | $11.568 \pm 0.024$ | 2MASS |
| $K_s$ (mag).......... | $11.479 \pm 0.022$ | $11.511 \pm 0.025$ | 2MASS |
| Derived properties | | | |
| $M_\star$ ($M_\odot$).......... | $1.030 \pm 0.039$ | $1.101 \pm 0.054$ | YY+$\rho_\star$+ZASPE [e] |
| $R_\star$ ($R_\odot$).......... | $1.503^{+0.101}_{-0.043}$ | $1.105^{+0.055}_{-0.040}$ | YY+$\rho_\star$+ZASPE |
| $\log g_\star$ (cgs) ........ | $4.095 \pm 0.038$ | $4.392 \pm 0.032$ | YY+$\rho_\star$+ZASPE |
| $\rho_\star$ (g cm$^{-3}$)........ | $0.427^{+0.030}_{-0.070}$ | $1.15^{+0.12}_{-0.16}$ | YY+$\rho_\star$+ZASPE [f] |
| $L_\star$ ($L_\odot$)........... | $1.70^{+0.24}_{-0.16}$ | $1.31 \pm 0.18$ | YY+$\rho_\star$+ZASPE |
| $M_V$ (mag)........ | $4.33 \pm 0.15$ | $4.52 \pm 0.16$ | YY+$\rho_\star$+ZASPE |
| $M_K$ (mag,ESO).... | $2.49 \pm 0.13$ | $3.05 \pm 0.10$ | YY+$\rho_\star$+ZASPE |
| Age (Gyr) ........ | $10.8 \pm 1.5$ | $3.3 \pm 1.7$ | YY+$\rho_\star$+ZASPE |
| $A_V$ (mag) ........ | $0.000 \pm 0.011$ | $0.112 \pm 0.075$ | YY+$\rho_\star$+ZASPE |
| Distance (pc) ...... | $622^{+42}_{-30}$ | $496 \pm 24$ | YY+$\rho_\star$+ZASPE |

[a]  ZASPE = **** routine for the analysis of high-resolution spectra (***cite***), applied to the FEROS spectra of HATS-9 and HATS-10. These parameters rely primarily on ZASPE, but have a small dependence also on the iterative analysis incorporating the isochrone search and global modeling of the data, as described in
[b]  Computed following Valenti & Fischer (2005).
[c]  Husser et al. (2013).
[d]  From APASS DR6 for HATS-9, HATS-10 as listed in the UCAC 4 catalog (Zacharias et al. 2012)..
[e]  YY+$\rho_\star$+ZASPE = Based on the YY isochrones (Yi et al. 2001), $\rho_\star$ as a luminosity indicator, and the ZASPE results.
[f]  In the case of $\rho_\star$ the parameter is primarily determined from the global fit to the light curves and RV data. The value shown here also has a slight dependence on the stellar models and ZASPE parameters due to restricting the posterior distribution to combinations of $\rho_\star + T_{eff\star}$+[Fe/H] that match to a YY stellar model.

The resulting parameters for each system are listed in Table 6. HATS-9b has a radius of $1.065 \pm 0.098 R_J$ and a mass of $0.837 \pm 0.029 M_J$, while HATS-10b has a radius of $0.969^{+0.061}_{-0.045} R_J$ and a mass of $0.526 \pm 0.081 M_J$. Both planets have bulk densities slightly lower than the one of Jupiter ($0.85 \pm 0.19$ g cm$^{-3}$ and $0.70 \pm 0.15$ g cm$^{-3}$, respectively)

### 4. DISCUSSION

We have presented the discovery of two new transiting planets which are shown on mass-radius and equilibrium temperature versus radius diagrams in Figure 7. From the mass-radius diagram, HATS-9b and HATS-10b can be classified as typical non-inflated hot Jupiters. HATS-9b is slightly less massive than Jupiter ($0.84 M_J$) and has almost the same radius. Its orbital period of $P = 1.9$ days is rather short compared to the period distribution

of known hot Jupiters. HATS-10b has a mass in the range between Saturn and Jupiter ($0.53 M_J$), a radius consistent with that of Jupiter and a period of $P = 3.3$ days, which is close to the mean period of known hot Jupiters.

The equilibrium temperature versus radius diagram shows that both planets tend to depart from the known correlation between the planet radius and its degree of irradiation. This correlation, first proposed in Guillot (2005), indicates that the inflated radius of some hot Jupiters can be at least partially explained by the enhanced insolation from their parent star. HATS-9b has a moderately high equilibrium temperature ($T_{eq}=1823^{+52}_{-35}$K) due to the small star-planet separation coupled to the large stellar radius, while HATS-10b has a more typical equilibrium temperature for a hot Jupiter

**Table 6**
Orbital and planetary parameters for HATS-9b and HATS-10b

| Parameter | HATS-9b Value | HATS-10b Value |
|---|---|---|
| **Light curve parameters** | | |
| $P$ (days) ..................... | $1.9153073 \pm 0.0000052$ | $3.3128460 \pm 0.0000058$ |
| $T_c$ (BJD) [a] ................... | $2456124.25896 \pm 0.00086$ | $2456457.88193 \pm 0.00022$ |
| $T_{14}$ (days) [a] ................. | $0.1457 \pm 0.0024$ | $0.1253 \pm 0.0011$ |
| $T_{12} = T_{34}$ (days) [a] .......... | $0.0106 \pm 0.0015$ | $0.01157 \pm 0.00100$ |
| $a/R_\star$ ........................ | $4.36^{+0.10}_{-0.25}$ | $8.73^{+0.29}_{-0.44}$ |
| $\zeta/R_\star$ [b] ........................ | $14.84 \pm 0.26$ | $17.588 \pm 0.067$ |
| $R_p/R_\star$ ........................ | $0.0725 \pm 0.0041$ | $0.0903 \pm 0.0013$ |
| $b^2$ ........................... | $0.071^{+0.112}_{-0.050}$ | $0.113^{+0.087}_{-0.059}$ |
| $b \equiv a \cos i/R_\star$ ............... | $0.27^{+0.16}_{-0.12}$ | $0.34^{+0.11}_{-0.10}$ |
| $i$ (deg) ...................... | $86.5^{+1.6}_{-2.5}$ | $87.79 \pm 0.72$ |
| **Limb-darkening coefficients [c]** | | |
| $c_1, g$ (linear term) ........... | $\cdots$ | $0.5380$ |
| $c_2, g$ (quadratic term) ........ | $\cdots$ | $0.2487$ |
| $c_1, r$ ......................... | $0.4688$ | $0.3459$ |
| $c_2, r$ ......................... | $0.2596$ | $0.3349$ |
| $c_1, i$ ......................... | $0.3533$ | $0.2587$ |
| $c_2, i$ ......................... | $0.2892$ | $0.3388$ |
| $c_1, z$ ......................... | $\cdots$ | $0.1978$ |
| $c_2, z$ ......................... | $\cdots$ | $0.3360$ |
| $c_1, R$ ......................... | $0.4369$ | $0.3216$ |
| $c_2, R$ ......................... | $0.2687$ | $0.3371$ |
| **RV parameters** | | |
| $K$ (m s$^{-1}$) ................... | $133.5 \pm 3.4$ | $67 \pm 10$ |
| $e$ [d] ........................... | $< 0.129$ | $< 0.501$ |
| RV jitter HDS (m s$^{-1}$) [e] ...... | $0.1 \pm 5.2$ | $0.00 \pm 0.53$ |
| RV jitter FEROS (m s$^{-1}$) .... | $0.0 \pm 1.7$ | $38 \pm 28$ |
| RV jitter Coralie (m s$^{-1}$) ..... | $0.0 \pm 1.1$ | $45 \pm 23$ |
| **Planetary parameters** | | |
| $M_p$ ($M_{\rm J}$) ..................... | $0.837 \pm 0.029$ | $0.526 \pm 0.081$ |
| $R_p$ ($R_{\rm J}$) ..................... | $1.065 \pm 0.098$ | $0.969^{+0.061}_{-0.045}$ |
| $C(M_p, R_p)$ [f] ................. | $0.48$ | $0.02$ |
| $\rho_p$ (g cm$^{-3}$) ................. | $0.85 \pm 0.19$ | $0.70 \pm 0.15$ |
| $\log g_p$ (cgs) ................... | $3.253 \pm 0.068$ | $3.140 \pm 0.082$ |
| $a$ (AU) ....................... | $0.03048 \pm 0.00038$ | $0.04491 \pm 0.00074$ |
| $T_{\rm eq}$ (K) ...................... | $1823^{+52}_{-35}$ | $1407 \pm 39$ |
| $\Theta$ [g] .......................... | $0.0460 \pm 0.0039$ | $0.0440 \pm 0.0071$ |
| $\log_{10}\langle F \rangle$ (cgs) [h] .............. | $9.397^{+0.049}_{-0.033}$ | $8.947 \pm 0.047$ |

[a] Times are in Barycentric Julian Date calculated directly from UTC *without* correction for leap seconds. $T_c$: Reference epoch of mid transit that minimizes the correlation with the orbital period. $T_{14}$: total transit duration, time between first to last contact; $T_{12} = T_{34}$: ingress/egress time, time between first and second, or third and fourth contact.
[b] Reciprocal of the half duration of the transit used as a jump parameter in our MCMC analysis in place of $a/R_\star$. It is related to $a/R_\star$ by the expression $\zeta/R_\star = a/R_\star(2\pi(1 + e \sin \omega))/(P\sqrt{1 - b^2}\sqrt{1 - e^2})$ (Bakos et al. 2010).
[c] Values for a quadratic law, adopted from the tabulations by Claret (2004) according to the spectroscopic (ZASPE) parameters listed in Table 5.
[d] As discussed in Section 3.3 the adopted parameters for all four systems are determined assuming circular orbits. We also list the 95% confidence upper limit on the eccentricity determined when $\sqrt{e} \cos \omega$ and $\sqrt{e} \sin \omega$ are allowed to vary in the fit.
[e] Term added in quadrature to the formal RV uncertainties for each instrument. This is treated as a free parameter in the fitting routine.
[f] Correlation coefficient between the planetary mass $M_p$ and radius $R_p$ estimated from the posterior parameter distribution.
[g] The Safronov number is given by $\Theta = \frac{1}{2}(V_{\rm esc}/V_{\rm orb})^2 = (a/R_p)(M_p/M_\star)$ (see Hansen & Barman 2007).
[h] Incoming flux per unit surface area, averaged over the orbit.

($T_{\rm eq}$=1407 ± 39K). According to the empirical relations proposed in Enoch et al. (2012), which give the radius of a giant planet from its equilibrium temperature and semi-major axis, HATS-9b and HATS-10b should have radii of $1.36R_{\rm J}$ and $1.22R_{\rm J}$, respectively. The observed radii are $3\sigma$ and $5\sigma$ below these values, which indicates that these planets are very compact given their irradiation levels and that thus additional variables must be responsible of setting the radii of short period giant planets.

One possible explanation is that HATS-9b and HATS-

10b may have significant amounts of heavy elements in their cores. According to the interior models of Fortney et al. (2007), both planets will require a core mass of $\sim$60 $M_\oplus$ to explain their radii based on their masses, stellar host masses and orbital periods for an age of 4.5 Gyr. This explanation can be further motivated by the relatively high metallicity of their parent stars ($0.340 \pm 0.050$ dex and $0.15 \pm 0.10$ dex, respectively). Several works (Guillot et al. 2006; Burrows et al. 2007; Enoch et al. 2011, 2012) have proposed a correlation between the inferred core mass of giant planets and the metallicity of

the parent star. The principal idea behind the proposed correlation is that a more metal rich proto-planetary disk will be more efficient in creating massive cores following the core-accretion scenario of planetary formation. Even though this process is expected to occur in the formation and migration steps, the final relation between the stellar metallicity and the radius of giant planets is not at all clear and other phenomena can act in the opposite direction. As shown by Burrows et al. (2007), the presence of heavy elements in the atmosphere of young giant planets will increase its opacity, slowing the contraction and making the planetary radius more inflated than expected. Moreover, the validity of the proposed correlation has been put into question by the analysis Zhou et al. (2014a) who find no significant correlation between $R_p$ and [Fe/H] for the complete sample of detected giant TEPs.

The age of the system may be another important variable, since the radius of giant planets should undergo Kelvin-Helmholtz contraction as they age, controlled by their upper radiative atmosphere (Hubbard 1977). Figure 8 presents the mass-radius diagram of transiting hot Jupiters having similar insolation levels to HATS-9b ($1750K < T_{eq} < 1900K$). This figure shows that in general the bloating of the atmosphere of strongly irradiated planets is prevented for more massive hot Jupiters. This correlation presents some outliers, with HATS-9b the most extreme one. A peculiarity of HATS-9b is the advanced age of the system ($\sim$11 Gyr) contrasted with the ages of the rest of the planets in Figure 8 ($<$5 Gyr). Among the complete sample of well characterized hot Jupiters, HATS-9b and CoRoT-17 b ($10.7 \pm 1.0$ Gyr) are the oldest systems known to have an age uncertainty better than 20%. Figure 9 shows the radius as function of age for hot Jupiters with $0.5 M_J < M_p < 2 M_J$ and orbital period P $< 10$ days having age uncertainties smaller than 40%. Systems older than 3 Gyr exhibit the expected contraction of the envelope through time but most of them are systematically more inflated than expected from theoretical models of structure and evolution. By fitting a straight line through the planets with ages higher than 3 Gyr we obtain an empirical contraction function for hot Jupiters: $R_p = 1.45 - 0.03t$, where $t$ is the age of the system in Gyr. The difference between the theoretical function and the empirical relation decreases with the age of the system and for the case of HATS-9b both functions are consistent with the observed values. The proposed empirical relation between the age of the system and the radius of the planet shown in Figure 9 supports the study of Burrows et al. (2007) where for young giant planets the higher opacity produced by heavy elements delays the contraction, while at later ages the higher mean molecular weight dominates and leads to smaller radii. However, in order to perform a precise study of the evolution of the the radii of giant extrasolar planets, particular models with the properties of each system should be constructed.

A possible confusing factor in Figures 7, 8 and 9 is the assumption of zero albedo and complete heat redistribution. The measurement of secondary transits on these systems in different wavelengths will be informative for explaining the departure of HATS-9b from the correlation. A more precise determination of the radius of HATS-9b is also required. The somewhat larger uncer-

tainty in the radius is a result of the incomplete photometric follow-up for this system. The errors in the planet radius are governed at this point by the light-curve data, but future precise measurements of the transit of HATS-9b will be able to lower this uncertainty until it becomes dominated by the uncertainties on the stellar parameters.

Future precise RV measurements of HATS-10b are required to determine a more precise mass of the planet and to explain the high jitter measured with FEROS and Coralie with respect to Subaru/HDS. One possible explanation may be the presence of another planetary companion. Subaru/HDS observations, which don't seem to show enhanced jitter, were performed in three continuous days, while Coralie and FEROS observations were separated by months and in this case the influence of a second more distant companion should be stronger. The jitter values quoted in Table 6 refer to RV uncertainties for each instrument that have to be added in quadrature to the formal RV errors in order for them to be consistent with the RV signal computed with the orbital parameters of the system.

### 4.1. *K2 possibilities*

Even thought HATS-9b and HATS-10b are located in the nominal coordinates of field 7 of K2, only HATS-9b falls on working silicon. A proposal to observe this star in short cadence was recently submitted. The high photometric precision of K2 will allow us to estimate a much more precise radius for HATS-9b, which will help us in determining if this planet is a true outlier in the correlation between planet radius, equilibrium temperature and planet mass. The high insolation of this planet makes it a very good target for measuring secondary transits and phase curve variations with K2, which will allow us to estimate the albedo and provide a more reliable estimate of its equilibrium temperature. Figure 10 shows a measure of the reflected light signature , $(R_P/a)^2$, for hot Jupiters observed by *Kepler* as a function of planetary radius. From this Figure we can see that the potential of detecting reflected light signatures of HATS-9b is high and its amplitude should be similar to the one of the giant planets observed by *Kepler* so far. Other subtle photometric effects, like ellipsoidal variations, Doppler beaming and the measurement of asteroseismological frequencies, if present, will also be very valuable for the detailed characterization of this particular planet.

**Figure 7.** (Left): Mass-radius diagram of giant TEPs. HATS-9b is marked with a filled square and HATS-10b with a filled triangle. Isodensity curves are plotted with dashed lines for $\rho_P = \{0.25, 0.5, 1.0, 2.0, 4.0\}$ gr cm$^3$ and the 4.5 Gyr isochrones (Fortney et al. 2007) for core masses of 0 and 100 M$_\oplus$ with solid lines. (Right): Equilibrium temperature versus radius diagram for giant TEPs. Again, HATS-9b is marked with a filled square and HATS-10b with a filled triangle.
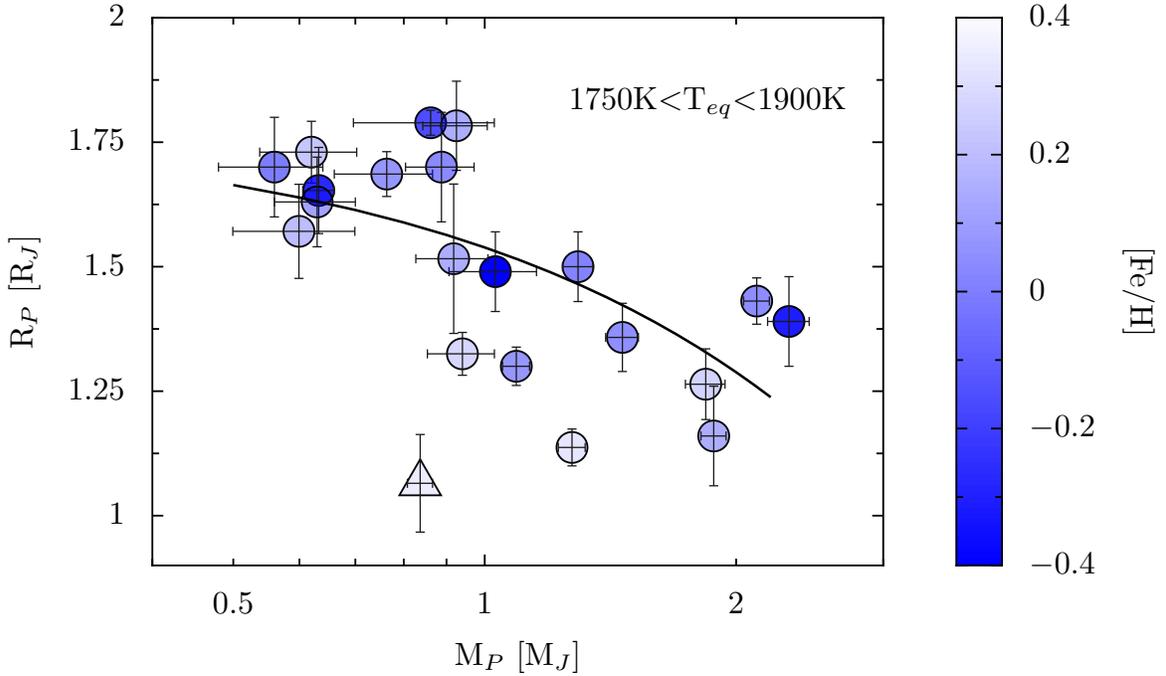


**Figure 8.** Mass-radius diagram of giant TEPs having similar insolation levels to HATS-9b (1750K< $T_{eq}$<1900K). HATS-9b is marked with a triangle. Filled symbols are colored according to the metallicity of the host star. HATS-9b does not follow the correlation formed by the other hot Jupiters with similar irradiation levels.

**Figure 9.** Radius as function of the age of the system for hot Jupiters having $0.5M_J < M_p < 2M_J$, P<10 days and an age estimation with a precision better than 40%. Green lines are the theoretical models of Fortney et al. (2007) for $M_p = 1M_J$, $a = 0.02$AU and a core mass of 0 (dashed) and 50 (solid) times the mass of the earth. The red line is an empirical relation computed with these data points. HATS-9b is marked with a triangle. Hot Jupiters older than 3 Gyr follow the contraction of their radius over time but the observed contraction rate is steeper than the one predicted from the theoretical models. The theoretical radii for Hot Jupiters with ages greater than 10 Gyr (like HATS-9b) is consistent with the observations.
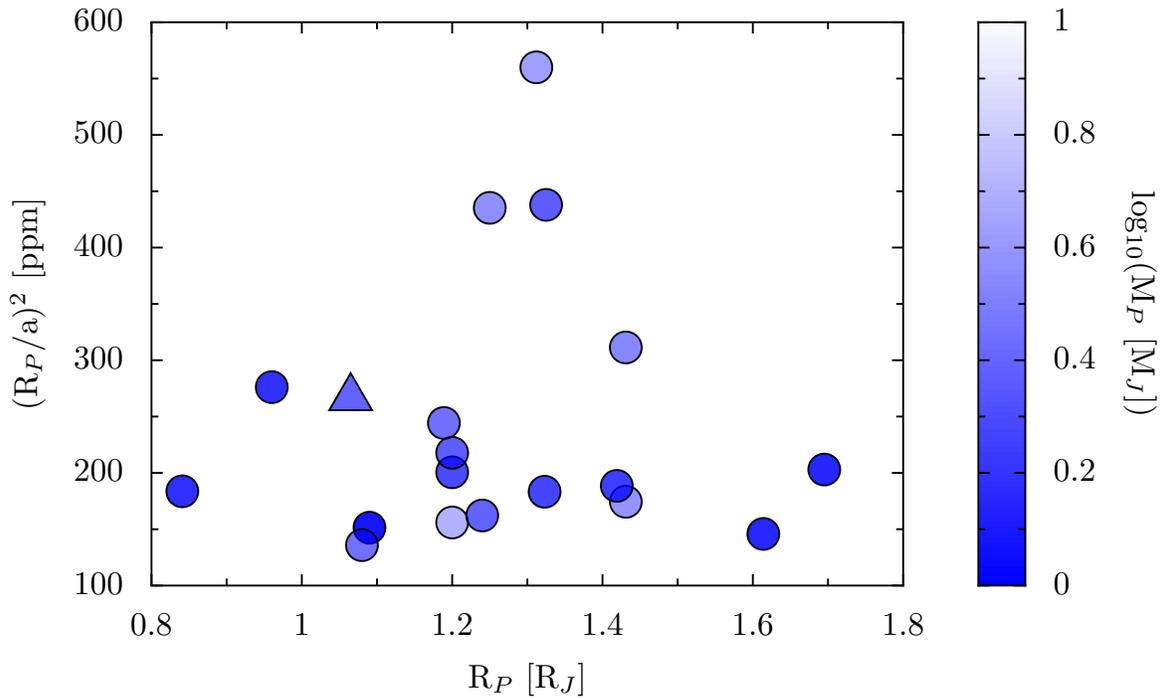


**Figure 10.** Reflected light signature as function of the planetary radius for the hot Jupiters observed with Kepler. The symbols are colored according to the planetary mass. HATS-9b is marked with a triangle. Given that the photometric precision of K2 is similar to the one of the original *Kepler* mission, phase curve variations and secondary the secondary transit of HATS-9b should be measured by K2.

## REFERENCES

Aigrain, S., Hodgkin, S. T., Irwin, M. J., Lewis, J. R., & Roberts, S. J. 2015, MNRAS, 447, 2880

Bakos, G., Noyes, R. W., Kovács, G., et al. 2004, PASP, 116, 266

Bakos, G. Á., Kovács, G., Torres, G., et al. 2007, ApJ, 670, 826

Bakos, G. Á., Torres, G., Pál, A., et al. 2010, ApJ, 710, 1724

Bakos, G. Á., Csubry, Z., Penev, K., et al. 2013, PASP, 125, 154

Bayliss, D., Zhou, G., Penev, K., et al. 2013, AJ, 146, 113

Borucki, W. J., Koch, D., Basri, G., et al. 2010, Science, 327, 977

Boyajian, T. S., McAlister, H. A., van Belle, G., et al. 2012, ApJ, 746, 101

Buchhave, L. A., Latham, D. W., Johansen, A., et al. 2012, Nature, 486, 375

Burrows, A., Hubeny, I., Budaj, J., & Hubbard, W. B. 2007, ApJ, 661, 502

Cardelli, J. A., Clayton, G. C., & Mathis, J. S. 1989, ApJ, 345, 245

Christensen-Dalsgaard, J., Kjeldsen, H., Brown, T. M., et al. 2010, ApJ, 713, L164

Claret, A. 2004, A&A, 428, 1001

Crossfield, I. J. M., Petigura, E., Schlieder, J. E., et al. 2015, ApJ, 804, 10

Deming, D., Sada, P. V., Jackson, B., et al. 2011, ApJ, 740, 33

Dopita, M., Hart, J., McGregor, P., et al. 2007, Ap&SS, 310, 255

Eastman, J., Gaudi, B. S., & Agol, E. 2013, PASP, 125, 83

Enoch, B., Collier Cameron, A., & Horne, K. 2012, A&A, 540, A99

Enoch, B., Cameron, A. C., Anderson, D. R., et al. 2011, MNRAS, 410, 1631

Esteves, L. J., De Mooij, E. J. W., & Jayawardhana, R. 2013, ApJ, 772, 51

Everett, M. E., Barclay, T., Ciardi, D. R., et al. 2015, AJ, 149, 55

Foreman-Mackey, D., Montet, B. T., Hogg, D. W., et al. 2015, ArXiv e-prints, 1502.04715

Fortney, J. J., Marley, M. S., & Barnes, J. W. 2007, ApJ, 659, 1661

Fraine, J., Deming, D., Benneke, B., et al. 2014, Nature, 513, 526

Guillot, T. 2005, Annual Review of Earth and Planetary Sciences, 33, 493

Guillot, T., Santos, N. C., Pont, F., et al. 2006, A&A, 453, L21

Hansen, B. M. S., & Barman, T. 2007, ApJ, 671, 861

Hartman, J. D., Bakos, G. Á., Torres, G., et al. 2011, ApJ, 742, 59

Hartman, J. D., Bakos, G. Á., Béky, B., et al. 2012, AJ, 144, 139

Hartman, J. D., Bayliss, D., Brahm, R., et al. 2014, ArXiv e-prints, 1408.1758

Horch, E. P., Howell, S. B., Everett, M. E., & Ciardi, D. R. 2014, ApJ, 795, 60

Howell, S. B., Everett, M. E., Sherry, W., Horch, E., & Ciardi, D. R. 2011, AJ, 142, 19

Howell, S. B., Sobeck, C., Haas, M., et al. 2014, PASP, 126, 398

Hubbard, W. B. 1977, icarus, 30, 305

Husser, T.-O., Wende-von Berg, S., Dreizler, S., et al. 2013, A&A, 553, A6

Jordán, A., Brahm, R., Bakos, G. Á., et al. 2014, AJ, 148, 29

Kaufer, A., & Pasquini, L. 1998, in Society of Photo-Optical Instrumentation Engineers (SPIE) Conference Series, Vol. 3355, Optical Astronomical Instrumentation, ed. S. D'Odorico, 844–854

Kovács, G., Bakos, G., & Noyes, R. W. 2005, MNRAS, 356, 557

Kovács, G., Zucker, S., & Mazeh, T. 2002, A&A, 391, 369

Mandel, K., & Agol, E. 2002, ApJ, 580, L171

Mohler-Fischer, M., Mancini, L., Hartman, J. D., et al. 2013, A&A, 558, A55

Noguchi, K., Aoki, W., Kawanomoto, S., et al. 2002, PASJ, 54, 855

O'Donovan, F. T., Charbonneau, D., Mandushev, G., et al. 2006, ApJ, 651, L61

Pál, A., Bakos, G. Á., Torres, G., et al. 2008, ApJ, 680, 1450

Penev, K., Bakos, G. Á., Bayliss, D., et al. 2013, AJ, 145, 5

Pollacco, D. L., Skillen, I., Collier Cameron, A., et al. 2006, PASP, 118, 1407

Queloz, D., Mayor, M., Udry, S., et al. 2001, The Messenger, 105, 1

Sanchis-Ojeda, R., & Winn, J. N. 2011, ApJ, 743, 61

Sozzetti, A., Torres, G., Charbonneau, D., et al. 2007, ApJ, 664, 1190

ter Braak, C. J. F. 2006, Statistics and Computing, 16, 239

Valenti, J. A., & Fischer, D. A. 2005, ApJS, 159, 141

Vanderburg, A., & Johnson, J. A. 2014, PASP, 126, 948

Yi, S., Demarque, P., Kim, Y.-C., et al. 2001, ApJS, 136, 417

Zacharias, N., Finch, C. T., Girard, T. M., et al. 2012, VizieR Online Data Catalog, 1322, 0

Zhou, G., Bayliss, D., Penev, K., et al. 2014a, ArXiv e-prints, 1401.1582

Zhou, G., Bayliss, D., Hartman, J. D., et al. 2014b, MNRAS, 437, 2831